International Journal of Refrigeration 134 (2022) 232–241

Contents lists available at ScienceDirect

International Journal of Refrigeration

journal homepage: www.elsevier.com/locate/ijrefrig

Analysis of hybrid compression absorption refrigeration using low-GWP HFC or HFO/ionic liquid working pairs

Analyse du froid hybride à absorption-compression utilisant des couples de travail HFC ou HFO/liquide ionique à faible PRP

José M. Asensio-Delgado, Salvador Asensio-Delgado, Gabriel Zarca, Ane Urtiaga *

Department of Chemical and Biomolecular Engineering, University of Cantabria, Av. Los Castros 46, Santander 39005, Spain

ARTICLE INFO

Keywords:
Hydrofluorocarbon
Hydrofluoroolefin
Absorption refrigeration
Thermodynamic modeling
R1234ze(E)
Ionic liquid

Mots clés:
Hydrofluorocarbure
Hydrofluoroléfine
Froid à absorption
Modélisation thermodynamique
R1234ze(E)
Liquide ionique

ABSTRACT

Absorption refrigeration systems (ARS) are the leading alternative for reducing the electricity costs associated with compression refrigeration systems. However, classical pairs based on NH_3/H_2O and H_2O/LiBr have drawbacks that limit their practical application. In this work, we analyze 16 pairs of refrigerant gases and ionic liquid sorbents based on two low global warming potential (GWP) hydrofluorocarbons (HFCs), R32 and R134a, and two novel hydrofluoroolefins (HFOs), R1234ze(E) and R1234yf, using the low-viscosity ionic liquids [C_2mim][BF_4], [C_2mim][OTf], [C_2mim][SCN], and [C_2mim][Tf_2N]. We provide new data and modeling of the vapor-liquid equilibria of R1234ze(E) with [C_2mim][OTf], [C_2mim][SCN] and [C_2mim][Tf_2N]. ARS performance in single-effect (SE-ARS) and compression-assisted absorption refrigeration (CA-ARS), in terms of coefficient of performance (*COP*, *ECOP*), solution circulation factor (f), and the thermal and electrical contribution to the total *COP*, is evaluated through energy and exergy analyses. The results showed that CA-ARS performs better even at lower generator temperatures. In addition, HFCs returned a better performance than HFOs because of their higher solubility in ILs. The working pair R32/[C_2mim][Tf_2N] gave the best results, $COP = 0.74$ and $f = 5.4$ at 328 K in the desorber, and a maximum *ECOP* of 0.41 at 318 K. Furthermore, the HFO R1234ze(E), with a lower working pressure and negligible GWP, is also a promising option for CA-ARS. In conclusion, we consider that ARS with the HFC or HFO/IL pairs examined in this study shows outstanding potential as a more energy efficient system compared to compression systems, when an inexpensive energy source is available.

1. Introduction

Modern global challenges encourage our society to develop a clean and carbon-neutral economy. In this context, the heating and cooling sector accounted for 51% of the total final energy consumption in the EU in 2012 and 27% of total greenhouse gas (GHG) emissions in Europe in 2018, making it the highest contributor ahead of road transportation (European Environment Agency, 2020; European Commission, 2020). Current refrigeration technology is mostly based on compression refrigeration systems (CRS), which have high power consumptions, e.g., up to 15% of the total electricity consumption in developed countries such as Germany (Seiler et al., 2013). To meet climate change objectives and reduce atmospheric pollution, more innovation and further research into energy-saving cooling technologies are required (Seiler et al., 2013; Garcia et al., 2021).

Absorption refrigeration systems (ARS) are alternatives to conventional compression refrigeration systems (CRS). ARS are powered by thermal energy rather than electricity, so the objective is to use low-grade energy from renewable sources, such as solar or geothermal energy, or from waste heat. Classical ARS use ammonia/water (NH_3/H_2O) and water/lithium bromide (H_2O/LiBr) as working pairs, although they have several disadvantages, namely, toxicity, flammability, the need for a rectifier to separate the NH_3 from the H_2O, high-temperature

Abbreviations: ARS, Absorption Refrigeration Systems; CA-ARS, Compression-Assisted Absorption Refrigeration Systems; CRS, Compression Refrigeration Systems; COP, Coefficient of Performance; ECOP, Exergy efficiency; GHG, Greenhouse Gas; GWP, Global Warming Potential; HFC, Hydrofluorocarbons; HFO, Hydrofluoroolefins; IL, Ionic liquids; NRTL, NonRandom Two-Liquid model; SE-ARS, Single-Effect Absorption Refrigeration Systems; VLE, Vapor-Liquid Equilibria.

* Corresponding author.
E-mail address: urtiaga@unican.es (A. Urtiaga).

https://doi.org/10.1016/j.ijrefrig.2021.11.013
Received 2 July 2021; Received in revised form 20 October 2021; Accepted 22 November 2021
Available online 24 November 2021

Nomenclature

B	Second virial coefficient, $m^3 \cdot mol^{-1}$
C	Gas concentration, $mol \cdot m^{-3}$
D	Diffusivity, $m^2 \cdot s^{-1}$
f	Circulation factor,
$\bar{f}$	Fugacity, MPa
h	Specific enthalpy, $kJ \cdot kg^{-1}$ or $kJ \cdot mol^{-1}$
k_H	Henry's law constant, MPa
m	Mass flow rate, $kg \cdot s^{-1}$
M_m	Molecular mass, $kg \cdot mol^{-1}$
p	Pressure, MPa
Q	Heat duty, kW
R	Ideal gas constant, $J \cdot mol^{-1} \cdot K^{-1}$
T	Temperature, K
V	Volume, L
w	Mass fraction,
W	Power, kW
x, y	Mole fraction,

Greek letters

$\alpha, \tau_{12}^0, \tau_{12}^1, \tau_{21}^0, \tau_{21}^1$	NRTL adjustable parameters
γ	Activity coefficient, -
μ	Dynamic viscosity, mPa·s
η_{hx}	Heat exchanger efficiency, -
ρ	Molar density, $mol \cdot L^{-1}$
Φ	Fugacity correction factor

Subscripts

c	condenser
comp	compressor
con	IL-concentrated solution
d	desorber or generator
dil	IL-diluted solution
e	evaporator
el	electrical
ex	excess
hx	heat exchanger
i, 1, 2…	component
p	pump
r	refrigerant
ref	reference
th	thermal
v	expansion valve

Superscripts

L	saturated liquid
S	saturated vapor
s	isentropic

corrosion, and operation at subatmospheric pressures or crystallization in the case of H_2O/LiBr (Seiler et al., 2013).

There are various approaches to overcome the main drawbacks of classical ARS including the application of new absorbents and hydrofluorocarbon refrigerants. Regarding the absorbents, some recent studies have analyzed the use of organic solvents, such as TEGDME (triethylene glycol dimethyl ether) or the synthetic polyolester oil PZ46M (Gao et al., 2019; Zhang et al., 2021). The use of ionic liquids (ILs) is also attracting attention thanks to their interesting properties, including an extremely low vapor pressure, high thermal and chemical stability, liquid stability over a wide temperature range, non-flammability and excellent solvation properties, among others -(Asensio-Delgado et al., 2021a). Some of these new IL absorbents have been studied in absorption pairs with NH_3 and H_2O (Yokozeki and Shiflett, 2010; Kim et al., 2012; Wang and Infante Ferreira, 2017; Moreno et al., 2018). However, the pairs containing NH_3 are still toxic, flammable, and corrosive, and the use of H_2O is limited at low evaporator temperatures. In this regard, the use of hydrofluorocarbon (HFC) refrigerants is expected to increase the range of viable operating temperatures and reduce the toxicity of ARS. Nontoxic HFCs are noted for their low or negligible flammability, stability and good thermodynamic properties (Asensio-Delgado et al., 2020a). However, some HFCs act as greenhouse gasses (GHGs) with a high global warming potential (GWP). This factor is driving the refrigeration sector towards the use of hydrofluoroolefins (HFOs), a group of compounds with a much lower GWP than HFCs and harmless to the ozone layer (McLinden and Huber, 2020). To date, only the performance of some fluorinated refrigerant/IL working pairs has been assessed in absorption refrigeration using, among others, R134a, R32, R152a, R161, R1234ze(E), or R1234yf refrigerants combined with [C_4mim][PF_6], [C_6mim][PF_6], [C_6mim][Tf_2N], [C_6mim][BF_4], or [C_6mim][OTf] ILs (Kim et al., 2012; Wu et al., 2018; Y. Sun et al., 2020; Y. Sun et al., 2020; Liu et al., 2019; Wu et al., 2020; W. Wu et al., 2017; W. Wu et al., 2017). However, with the exception of [C_6mim][Tf_2N], the ILs studied so far have viscosities higher than 100 mPa·s at 303.15 K. The high viscosity of the absorbents may reduce mass and energy transfer rates and increase pumping costs, thereby reducing the system's energy efficiency (Zarca et al., 2014; Zarca et al., 2015). So, we still need to learn more about ARS performance when using low-viscosity ILs together with HFCs and HFOs as working fluids.

ARS involve replacing the compressor of a CRS with an absorption—desorption cycle in which the refrigerant is first dissolved and then pressurized in liquid state, which is a more energy-efficient process than vapor compression given the lower specific volume (Seiler et al., 2013). After pumping, the refrigerant is released from the absorbent by heating the solution. This cycle is known as Single-Effect Absorption Refrigeration System (SE-ARS) and is shown schematically in Fig. 1a. Additionally, a solution heat exchanger is placed between the absorber and desorber to increase the cycle's thermal efficiency. However, the system may underperform if the heat source is too cool or the pressure in the absorber too low. To expand the range of viable operating conditions, the Compression-Assisted Absorption Refrigeration System (CA-ARS), a hybrid between CRS and SE-ARS, has also been proposed (Fig. 1b). In CA-ARS, the compressor is installed after the evaporator to increase the solubility in the absorber thanks to the higher inlet pressure. Consequently, CA-ARS does not eliminate the use of a compressor but substantially reduces its energy requirements.

In this work, we aimed to characterize the behavior of 16 working pairs formed from HFCs or HFOs with different low-viscosity ILs and analyze their refrigeration performance in SE-ARS and CA-ARS, which is a more demanding application than air conditioning for these thermally driven systems. We focused on two of the most widely used HFCs, R134a and R32, and the two HFOs that are attracting the most attention at the moment, R1234ze(E) and R1234yf. Table 1 contains their chemical names, molar masses and GWPs. The very low-viscosity ILs [C_2mim][BF_4], [C_2mim][OTf], [C_2mim][SCN], and [C_2mim][Tf_2N] were selected over more viscous ILs because it was expected their real performances would approach those predicted by the equilibrium analyses considering the higher heat and mass transfer rates. This hypothesis has already been tested for IL-based separation processes analyzed in rate-based models (Mota-Martinez et al., 2018; Palomar et al., 2019). We also assess the influence of the anion structure on ARS cycle performance. Table 2 presents the chemical names of these ILs as well as some properties of interest. The vapor-liquid equilibria (VLE) required for

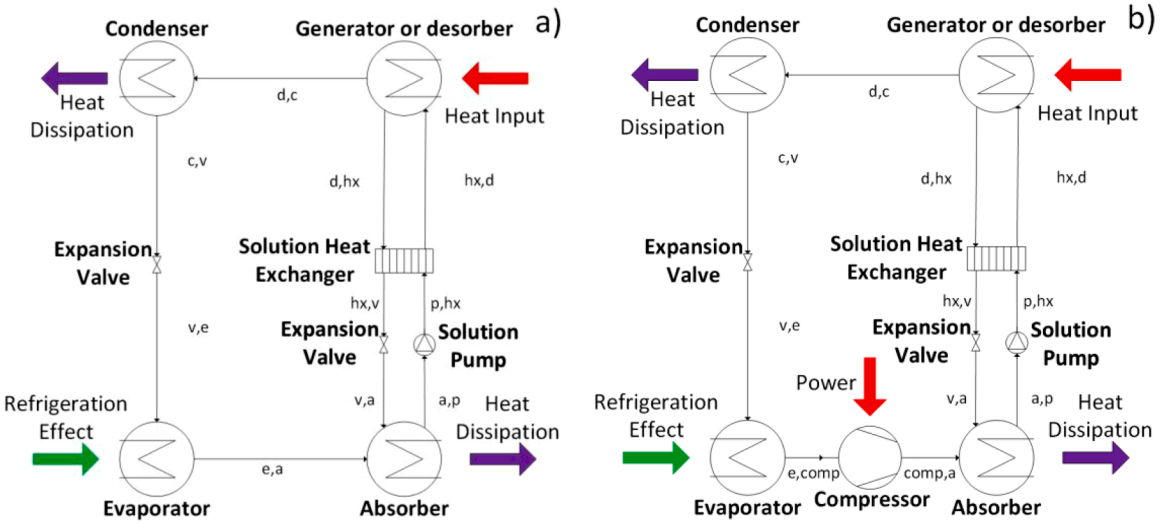

Fig. 1. Schematics of (a) a Single-Effect Absorption Refrigeration System (SE-ARS) and (b) a Compression-Assisted Absorption Refrigeration System (CA-ARS).

Table 1.
Refrigerants studied.

Type	Code	Name	M_m ($g \cdot mol^{-1}$)	GWP	T_c (K)
HFC	R134a	1,1,1,2-Tetrafluoroethane	102.03	1430	374.21
HFC	R32	Difluoromethane	52.02	675	351.26
HFO	R1234ze(E)	Trans-1,3,3,3-tetrafluoropropene	114.04	1	382.52
HFO	R1234yf	2,3,3,3-Tetrafluoropropene	114.04	1	367.85

Table 2.
Ionic liquids studied. Density and viscosity at 303.15 K (Sanmamed et al., 2010; Neves et al., 2013; Gardas et al., 2008; Freire et al., 2011; Součková et al., 2014; Atilhan et al., 2013).

Abbreviation	Name	M_m ($g \cdot mol^{-1}$)	ρ ($kg \cdot m^{-3}$)	μ (mPa·s)
[C_2mim][BF_4]	1-Ethyl-3-methylimidazolium tetrafluoroborate	197.97	1281.7	32.31
[C_2mim][OTf]	1-Ethyl-3-methylimidazolium trifluoromethanesulfonate	260.23	1370.0	35.98
[C_2mim][SCN]	1-Ethyl-3-methylimidazolium thiocyanate	169.24	1113.9	20.79
[C_2mim][Tf_2N]	1-Ethyl-3-methylimidazolium bis(trifluoromethylsulfonyl) imide	391.31	1514.3	26.9

some of these systems have been studied previously, but there is no information available in the literature on the absorption of R1234ze(E) in [C_2mim][OTf], [C_2mim][SCN] or [C_2mim][Tf_2N]. To solve this gap, we experimentally determined the VLE of these systems. We used the nonrandom two-liquid (NRTL) model to describe the VLE of each absorption pair and then used it in the thermodynamic modeling of the cycles. Overall, this study provides insights into the performance of new refrigerant/IL pairs in SE-ARS and CA-ARS systems working with a wide range of low-grade heat sources (generator temperature of between 313 and 373 K) for refrigeration purposes (evaporator temperature of 278 K).

2. Experimental section

2.1. Materials

R1234ze(E) (99.9%) was supplied by Coproven Climatización (Gas Servei licensed supplier, Spain). The IL [C_2mim][SCN] (98 wt%) was purchased from IoLiTec, and ILs [C_2mim][OTf] (98 wt%) and [C_2mim][Tf_2N] (98 wt%) were purchased from Sigma-Aldrich. Before use, the three ILs were vacuum dried and their water content measured using the Karl Fischer titration and found to be < 100 ppm.

2.2. Experimental apparatus and procedure

We used an isochoric saturation method to quantify the absorption of R1234ze(E) in the selected ILs. The description and validation of the experimental system is detailed in previous works (Asensio-Delgado et al., 2020b). In brief, it consisted of a jacketed stirred tank reactor (Buchi, model Picoclave, 170 mL) fitted with a temperature and pressure transducer (Keller, series PAA-33X, 0.01% accuracy) and a Pt-100 temperature sensor connected to a cryothermostatic bath (Julabo, model F25–ME, $\pm$ 0.01 K). This chamber was connected to a storage cylinder of known volume (146 mL) with another temperature and pressure transducer.

The gas chamber was loaded with 30 to 40 g ($\pm$ 0.0001 g) of IL and degassed by applying a vacuum for a minimum of 6 h at 333 K. In this setup, both gas solubility and diffusivity were obtained in a single experiment. After measuring the initial pressure and temperature of the gas-filled storage, the absorption process was allowed to proceed spontaneously for 20 min in order to make the diffusivity data calculation. It was then stirred at 500 rpm and gas absorption proceeded until it reached equilibrium conditions, i.e., when the pressure remained constant for more than 20 min. Section S1 of the Supplementary Information explains the data treatment used to calculate the solubility and diffusivity.

3. Modeling

3.1. Process simulation

The single-effect (SE-ARS) and the hybrid compression assisted (CA-ARS) systems were simulated using Matlab. The evaporator temperature was set at 278.15 K and the dissipation temperature (condenser and absorber) at 303 K, representing conditions found in a refrigeration system. The following assumptions were considered in this work:

1 The system operates at steady state.
2 The absorber and generator outlet solutions are in equilibrium.
3 Heat losses, flow resistance, and pressure drops are not considered.
4 The expansion valves produce isenthalpic pressure decrements.
5 The liquid and vapor phases are in the saturated state.
6 The efficiency of the solution heat exchanger is set at 0.8.
7 Following ASHRAE considerations (ASHRAE, 2013), the temperature of the refrigerant leaving the generator (*d,c*) is the same as that of the solution inlet (*hx,d*).
8 The compressor isentropic efficiency and compression ratio (CR) are set at 0.7 and 1.5, respectively (Wu et al., 2018).

The mass and energy balances Eqs. (1) to ((9)) must be solved simultaneously for each element in the system to determine the thermodynamic performance. The enthalpy subscripts indicate the equipment a stream comes from and goes to, e.g., $h_{d,c}$ represents the specific enthalpy of the stream that comes from the desorber and goes to the condenser. In addition, $h_{(comp,a),s}$ is the ideal enthalpy of the stream leaving the compressor.

$$Q_g + m_r f h_{hx,d} = m_r h_{d,c} + m_r (f-1) h_{d,hx} \tag{1}$$

$$Q_a + m_r f h_{a,p} = m_r h_{comp,a} + m_r (f-1) h_{v,a} \tag{2}$$

$$Q_c - m_r h_{c,v} = m_r h_{d,c} \tag{3}$$

$$Q_e - m_r h_{v,e} = m_r h_{e,ecomp} \tag{4}$$

$$m_r f h_{p,hx} = m_r f h_{a,p} + W_p \Rightarrow h_{b,hx} = h_{a,b} \tag{5}$$

$$W_{comp} = m_r \left(h_{comp,a} - h_{e,a}\right) = \frac{m_r \left(h_{(comp,a),s} - h_{e,a}\right)}{\eta_i} \tag{6}$$

$$p_a = p_e \ CR \tag{7}$$

$$Q_{hx} = m_r (f-1)\left(h_{d,hx} - h_{hx,v}\right) = m_r (f-1)\left(h_{hx,d} - h_{b,hx}\right) \tag{8}$$

$$\eta_{hx} = \frac{T_{hx,d} - T_{b,hx}}{T_{d,hx} - T_{b,hx}} \tag{9}$$

The thermodynamic properties of the refrigerants were obtained using CoolProp 6.4.0 software (Bell et al., 2014). The specific enthalpy of the solution can be calculated from:

$$h = x_1 h_1 + x_2 h_2 + h_{ex} \tag{10}$$

where x_1 and x_2 are the refrigerant and absorbent molar fractions, and h_{ex} is the excess enthalpy of the mixture calculated from the NRTL parameters:

$$h_{ex} = -RT^2 \left[x_1 \left(\frac{\partial \ln \gamma_1}{\partial T} \right)_{p,x} + x_2 \left(\frac{\partial \ln \gamma_2}{\partial T} \right)_{p,x} \right] \tag{11}$$

The enthalpies of the ILs were obtained from their heat capacities, which were fitted to a quadratic expression from experimental data (Waliszewski et al., 2005; Diedrichs and Gmehling, 2006; Zorębski et al., 2018) as shown in Section S2 of the Supplementary Information.

ARS performance is based on the refrigerant mass fraction difference (Δw) between the absorber (w_{dil}) and desorber (w_{con}). To study this effect, the circulation factor (f) is defined as the ratio between the solution mass flow leaving the absorber (m_{dil}) and the refrigerant mass flow used in the evaporator (m_r). This parameter is calculated from the mass balance on the refrigerant.

$$f = \frac{m_{dil}}{m_r} = \frac{1 - w_{con}}{\Delta w} = \frac{1 - w_{con}}{w_{dil} - w_{con}} \tag{12}$$

In addition to the circulation factor, other metrics can be used to evaluate the efficiency of these systems, namely, the coefficients of performance (*COPs*). *COPs* are defined as the amount of heat removed divided by the sum of the required energy and power input.

$$COP = \frac{Q_e}{Q_g + W_{comp}} \tag{13}$$

In CA-ARS, it is recommendable to evaluate partial *COPs* that consider the efficiency in function of the energy source, i.e., the electrical or mechanical COP_{el} that analyzes the power used in the compressor and pump, and the thermal COP_{th} that is used to compare absorption cycle thermodynamics and calculate the heat needed in the generator.

$$COP_{el} = \frac{Q_e}{W_{comp}} \tag{14}$$

$$COP_{th} = \frac{Q_e}{Q_g} \tag{15}$$

In addition, the efficiency of energy usage according to the second law of thermodynamics is measured with the exergy coefficient of performance (*ECOP*). Exergy is defined as the maximum useful power that can be produced by a system or flow (Takalkar et al., 2019). A reference ambient temperature is set (298.15 K in this work) and the exergy is measured as the system's deviation from equilibrium within this environment. For an ARS, the *ECOP* is defined as the ratio between the evaporator exergy and the exergy inputs.

$$ECOP = \frac{Q_e \left| 1 - \frac{T_{ref}}{T_e} \right|}{Q_g \left(1 - \frac{T_{ref}}{T_g} \right) + W_{comp}} \tag{16}$$

To verify the accuracy of the thermodynamic model's description of ARS, we compared our results for the working pair R1234ze(E)/[C_2mim][BF_4] with those published in the literature under the same conditions (Wu et al., 2018). Fig. S2 in the Supplementary Information shows that both SE-ARS and CA-ARS were reproduced to a high accuracy.

3.2. NRTL solubility model

An accurate absorption model is a crucial tool in the design of ARS. This study calculates the parameters for the nonrandom two-liquid (NRTL) model for the VLE of R1234ze(E) with [C_2mim][OTf], [C_2mim][SCN] and [C_2mim][Tf_2N]. The model is based on the use of activity coefficients and the VLE expression is given by

$$y_i \Phi p = x_i \gamma_i p_i^S \ (i \ \epsilon \ \mathbb{Z} \ [1, N]) \tag{17}$$

where γ_i is the activity coefficient, p_i^S the saturation pressure and Φ the correction factor, which is obtained from:

$$\Phi = \exp\left[\frac{\left(B_i - V_i^L\right)\left(p - p_i^S\right)}{RT} \right] \tag{18}$$

where B_i is the second virial coefficient and V_i^L is the saturated liquid molar volume, both obtained using CoolProp 6.4.0 software Bell et al., 2014). Combining Eqs. (17) and ((18), and as $y_i = 0$ due to the non-volatile character of ILs, the activity coefficient is:

$$\gamma_1 = \frac{p}{x_1 p_1^S} \exp\left[\frac{\left(B_1 - V_1^L\right)\left(p - p_1^S\right)}{RT} \right] \tag{19}$$

The optimized model parameters were obtained by minimizing the difference between the experimental activity coefficients and the values calculated with the NRTL model:

$$\ln \gamma_1 = x_2^2 \left[\tau_{21} \left(\frac{G_{21}}{x_1 + x_2 G_{21}} \right)^2 + \frac{\tau_{12} G_{12}}{\left(x_2 + x_1 G_{12}\right)^2} \right] \tag{20}$$

The $G_{12}, G_{21}, \tau_{12}$ and τ_{21} parameters are expressed as

$$G_{12} = \exp(-\alpha\tau_{12}) \quad G_{21} = \exp(-\alpha\tau_{21}) \tag{21}$$

$$\tau_{12} = \tau_{12}^0 + \frac{\tau_{12}^1}{T} \quad \tau_{21} = \tau_{21}^0 + \frac{\tau_{21}^1}{T} \tag{22}$$

where $\alpha, \tau_{12}^0, \tau_{12}^1, \tau_{21}^0$ and τ_{21}^1 are the model adjustable parameters.

4. Results and discussion

4.1. Experimental VLE, NRTL modeling and diffusivity

This section addresses the absorption of R1234ze(E) in [C_2mim][Tf_2N], [C_2mim][OTf], and [C_2mim][SCN]. The solubility data, measured at temperatures of between 283.15 and 323.15 K and pressures up to 0.35 MPa, are compiled in Tables S2-S4 of the Supplementary Information and plotted in Fig. 2. As can be seen, the amount of dissolved R1234ze(E) is much higher in [C_2mim][Tf_2N] and [C_2mim][OTf] than in [C_2mim][SCN] at the same temperature and pressure. The very low solubility of R1234ze(E) in [C_2mim][SCN] can be ascribed to the absence of fluorine moieties and weaker molecular interactions between R1234ze(E) and the $[SCN]^-$ anion.

The results also show that the NRTL model accurately described the VLE of mixtures of R1234ze(E) with ILs, where the absolute average relative deviations between experimental and calculated activity coefficients were 5.00%, 2.41%, and 5.95% for [C_2mim][Tf_2N], [C_2mim][OTf], and [C_2mim][SCN], respectively. The optimized binary interaction parameters are presented in Table 3, as well as the parameters for every other absorption pair studied in this work. The NRTL model was unavailable for some systems, denoted by an asterisk in Table 3, so we fitted experimental data from the literature to find the NRTL parameters.

The gas diffusion coefficients for R1234ze(E) at infinite dilution from 283.15 to 323.15 K are provided in Table 4. The gas diffusivity increases at higher temperatures and was very similar for [C_2mim][Tf_2N] and [C_2mim][OTf], while the diffusion coefficients for [C_2mim][SCN] were higher. These values are consistent with diffusion coefficients published for R134a and R1234yf in the same ILs ; (Asensio-Delgado et al., 2021b; Asensio-Delgado et al., 2020c). These are the first values for R1234ze(E) diffusivity reported in this type of solvent, so the results cannot be compared to the diffusion coefficients in more viscous ILs, but the use of these low-viscosity ILs is expected to provide higher mass transfer rates. For example, the diffusion coefficient for R1234yf in [C_2mim][OTf] is twice the diffusion coefficient in the more viscous [C_6mim][OTf] (S. Asensio-Delgado et al., 2020; He et al., 2017). Low viscosity helps decrease the resistance to flow (Asensio-Delgado et al., 2021b), so low-viscosity ILs should perform better than other ILs because of both increased mass transfer rates and reduced pump power consumption. The need for experimental diffusion coefficients has been brought up previously (Kühn et al., 2020), as these parameters would help us develop more accurate models that consider mass transfer resistances in the absorber and desorber.

4.2. Performance of refrigerant/IL working pairs in SE-ARS

This section looks at the performance of the 16 refrigerant/low-viscosity IL working pairs in SE-ARS. Fig. 3 shows the *COP* calculated for each working pair as a function of generator temperature, which ranged between 333 K and 373 K, except for refrigerants with a lower

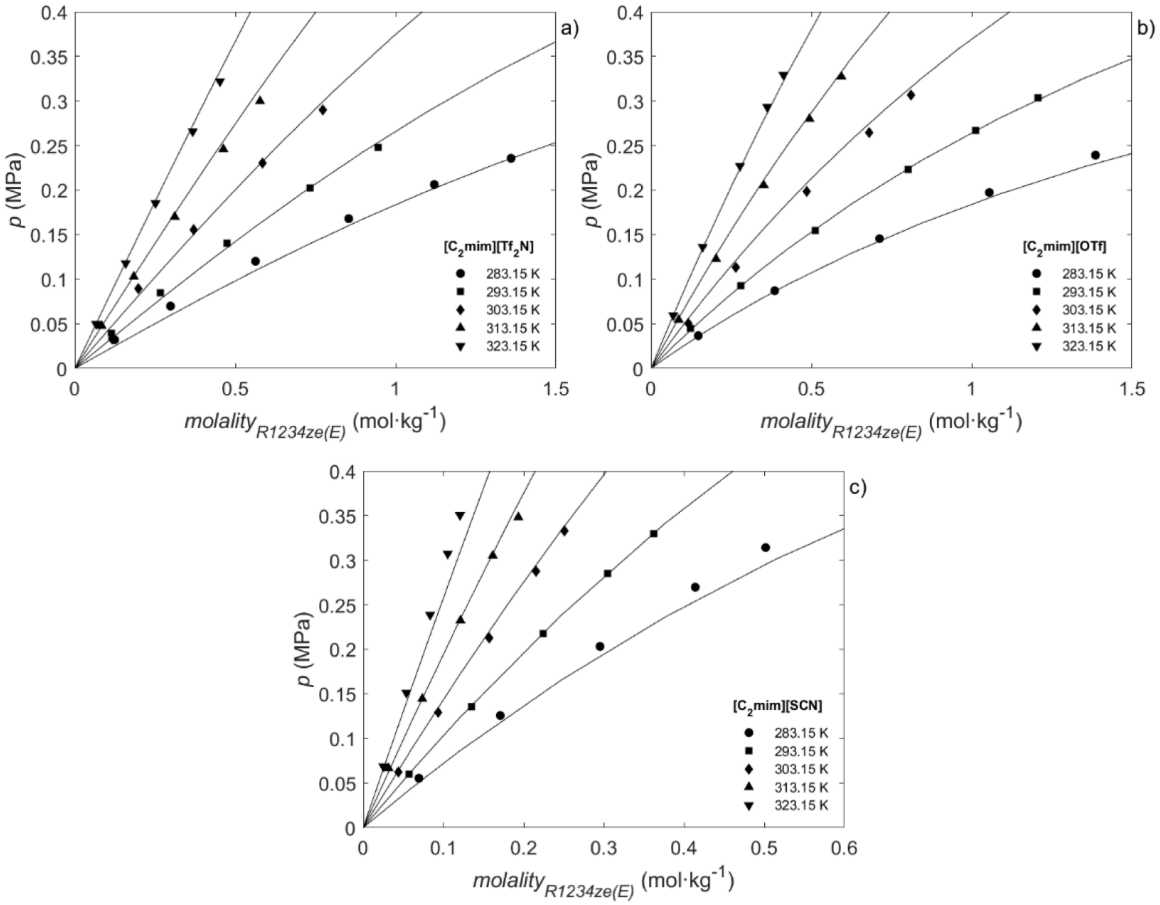

Fig. 2. Solubility of R1234ze(E) in (a) [C_2mim][Tf_2N], (b) [C_2mim][OTf] and (c) [C_2mim][SCN] at various temperatures: 283.15 (●), 293.15 (■), 303.15 (◆), 313.15 (▲), and 323.15 K (▼). Solid lines represent NRTL model calculations.

Table 3.
NRTL model parameters for each refrigerant/IL working pair.

Refrigerant	IL	α	τ_{12}^0	τ_{12}^1	τ_{21}^0	τ_{21}^1	Source
R134a	[C_2mim][BF_4]	0.2	0	4794.7	0	278.9	(Asensio-Delgado et al., 2020b)
	[C_2mim][OTf]	0.2	0	5076.4	0	99.29	(Asensio-Delgado et al., 2020b)
	[C_2mim][SCN]	0.2	0	2682.6	0	254.58	(Asensio-Delgado et al., 2020c)
	[C_2mim][Tf_2N]*	0.2	0	969.496	0	−443.388	(Shiflett and Yokozeki, 2007)
R32	[C_2mim][BF_4]	0.2	0	6148.1	0	51.99	(Asensio-Delgado et al., 2020b)
	[C_2mim][OTf]	0.24	−0.32	1259.4	−0.912	−145.71	(Dong et al., 2011)
	[C_2mim][SCN]	0.2	0	1025.6	0	−210.04	(Asensio-Delgado et al., 2020c)
	[C_2mim][Tf_2N]	0.2	0	959.31	0	−621.18	(Shiflett et al., 2006)
R1234ze(E)	[C_2mim][BF_4]	0.22	44.33	−10,698.57	6.8	−1805.14	(Wu et al., 2018)
	[C_2mim][OTf]	0.2	0	3782.794	0	97.713	This work
	[C_2mim][SCN]	0.2	4.056	372.699	2.458	−428.676	This work
	[C_2mim][Tf_2N]	0.2	0	3083.775	0	−175.027	This work
R1234yf	[C_2mim][BF_4]*	0.2	0	3238.731	0	596.401	(Sun et al., 2017)
	[C_2mim][OTf]	0.2	6.226	414.6	4.338	−1126.1	(Asensio-Delgado et al., 2020b)
	[C_2mim][SCN]	0.2	179.52	−47,781	21.89	−5506.8	(Asensio-Delgado et al., 2020c)
	[C_2mim][Tf_2N]	0.2	0	3844.6	0	135.2	(Asensio-Delgado et al., 2020b)

*NRTL model parameters optimized in this work.

Table 4.
R1234ze(E) diffusion coefficients (10^{-10} $m^2 \cdot s^{-1}$) at infinite dilution.

T (K)	[C_2mim] [Tf_2N]	[C_2mim] [OTf]	[C_2mim] [SCN]
283.15	0.42 ± 0.01	0.48 ± 0.01	1.2 ± 0.1
293.15	0.55 ± 0.02	0.60 ± 0.02	2.0 ± 0.2
303.15	1.05 ± 0.03	1.03 ± 0.03	2.6 ± 0.2
313.15	2.21 ± 0.06	2.18 ± 0.06	4.8 ± 0.4
323.15	4.0 ± 0.1	3.3 ± 0.1	11.3 ± 1.1

critical temperature (see Table 1). The *COP* behavior was very similar for almost every pair, with an initial increase in the *COP* at low temperatures thanks to a rapid decrease in refrigerant solubility in the generator, followed by a sluggish decrease due to the asymptotic value of the mass fraction difference between the generator and absorber observed at high generator temperatures. The exception was R1234yf in [C_2mim][SCN], owing to its very low solubility at all generator temperatures.

The best performances in SE-ARS were achieved using R32 with [C_2mim][BF_4], reaching a *COP* slightly over 0.4 with a generator temperature of around 350 K, similar to the values obtained in other studies for R32, R152a and R161 with [C_6mim][Tf_2N] (Wu et al., 2020). The next best IL was [C_2mim][Tf_2N], for which the highest *COPs* were 0.4 for R32 at 350 K and 0.35 for R134a at 360 K. In contrast, the *COPs* obtained with [C_2mim][SCN] were considerably lower. Between the two HFCs, R32 exhibited higher *COPs* than R134a except in [C_2mim][OTf], an IL that stands out as a R134a solvent, thus providing a stable working pair resilient to generator temperatures variations and with *COP* values of between 0.25 and 0.31 from 335 to 370 K. On the other hand, HFCs clearly outperformed the HFOs pairs. The HFO R1234ze(E) yielded better results than R1234yf for all the HFOs/ILs pairs at almost every generator temperature. The HFO pairs with the best performances were R1234ze(E)/[C_2mim][Tf_2N] and R1234ze(E)/[C_2mim][OTf], yet with *COP* values of just slightly over 0.2.

The complete assessment of SE-ARS is presented in Section S5 of the Supplementary Information, including the exergy analysis, circulation factors, mass fraction increments, and a comparison of the performance of the 16 working pairs under the same operating conditions. Overall, the refrigerant/IL pairs did not perform very well in SE-ARS, so their practical use is limited for such low-temperature refrigeration purposes. In contrast, SE-ARS may be a suitable option when thermal energy is abundant and relatively inexpensive, and for applications requiring higher evaporator temperatures, such as air conditioning, where the *COP* is twice as high with the evaporator at 18 °C instead of 5 °C as shown in Fig. S7 if the Supplementary Information. However, for cases with low-temperature energy sources or when limited heat is available the use of more efficient configurations such as CA-ARS should be encouraged.

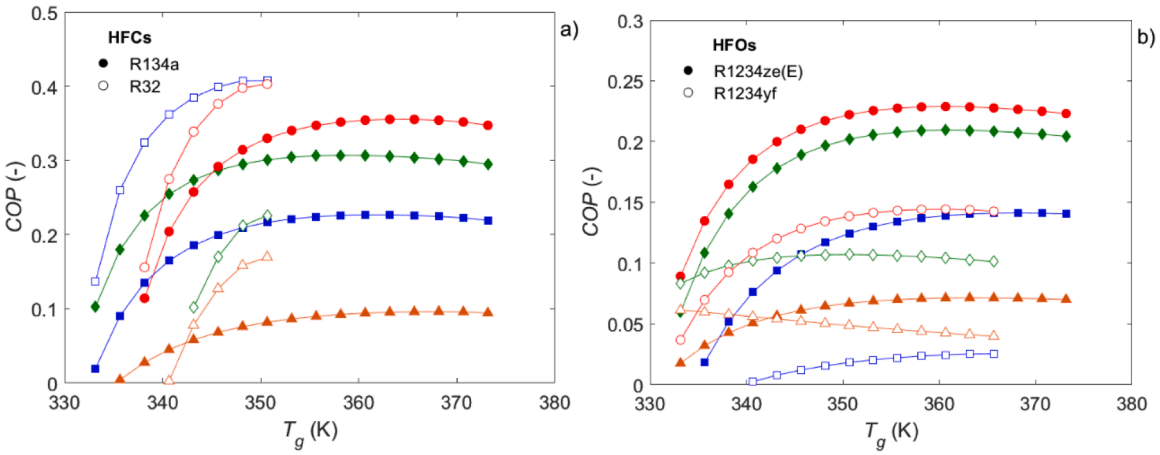

Fig. 3. *COP* of the SE-ARS systems as a function of generator temperature (T_g). (a) HFCs/IL: R134a (filled symbols) and R32 (empty symbols), and (b) HFOs/IL: R1234ze(E) (filled symbols) and R1234yf (empty symbols). Symbols represent the different ILs: [C_2mim][BF_4] (■), [C_2mim][OTf] (◆), [C_2mim][SCN] (▲), and [C_2mim][Tf_2N] (●). T_e = 278 K, $T_c = T_a$ = 303 K.

4.3. Performance of refrigerant/IL working pairs in CA-ARS

In CA-ARS, three *COPs* can be assessed in terms of the electricity input, the heat input, or both at the same time. As heat extraction in the evaporator does not vary with generator temperature, the electrical *COP* is constant for each refrigerant in all the working conditions studied regardless of the IL used, as it only depends on the vapor pressures of pure refrigerants at the operating temperatures, which are shown in Table S7 in the Supplementary Information. The electrical *COPs* are given in Table 5, which shows that the highest COP_{el} was that of R1234ze(E), followed by R134a, R1234yf, and R32.

As electrical usage was around ten times lower than the heat requirement, the thermal and total *COP* shared a similar variation with generator temperature, as shown in Fig. 4 and Fig. S8 in the Supplementary Information, in which the generator temperature ranged between 313 K and either 373 K or the refrigerant critical temperature (see Table 1). The working pair with the best performance was R32/[C_2mim][Tf_2N] with a COP_{th} of 0.79 and *COP* of 0.74 at 328 K. Out of the four ILs studied, [C_2mim][Tf_2N] stands out as the best absorbent for every refrigerant thanks to its high absorption capacity. In CA-ARS, HFCs again outperformed HFOs, but the combination of R1234ze(E) with [C_2mim][Tf_2N] or [C_2mim][OTf] may still hold some promise if enough waste heat is available at around 330 K. The working pairs studied in CA-ARS in this work performed better than HFC/IL working pairs assessed previously. For example, in the present study the pairs formed by R32 with [C_2mim][Tf_2N] and [C_2mim][OTf] yielded maximum *COP* values of over 0.7 at 328 K, while published pairs of R32, R152a and R161 with [C_6mim][Tf_2N] have peak performances below 0.68 at 328 K (Wu et al., 2020).

The *ECOP* calculated for the CA-ARS is shown in Fig. 5. For the HFO/IL pairs studied here, the maximum *ECOP* was approximately 0.24 at 323 K for the systems R1234ze(E)/[C_2mim][Tf_2N] and R1234ze(E)/[C_2mim][OTf], which is similar to literature data; for instance, the system R1234ze(E)/[C_6mim][Tf_2N] has been reported with a slightly higher *ECOP* of 0.26 (Wu et al., 2018). For the HFC/IL working pairs, the *ECOPs* obtained in this study are higher; for instance, the R32/IL and R134a/[C_2mim][Tf_2N] pairs reached peak values at between 0.41 and 0.3 in the temperature range 323—333 K.

The behavior of *COP* and *ECOP* was similar in SE-ARS and CA-ARS; it rose with increasing generator temperature up to a maximum value and then decreased. In CA-ARS, this increment was steeper and occurred at a lower generator temperature. The rationale behind this behavior can be found in the circulation ratio (f) plotted in Fig. 6, which shows an initial sharp decrease within a small range of generator temperatures, before stabilizing at an asymptotic value equal to the inverse of w_{dil} (i.e., when $w_{con} = 0$ in Eq. (18)). As the circulation ratio is derived from the dissolved mass fractions, the different changes in the *COP* values can be ascribed to the VLE, where ILs that absorb large amounts of refrigerant at low temperature and small amounts at high temperatures will afford the best performances. For CA-ARS, the lowest circulation factors reach values of 4—5 for both HFCs (R134a and R32) and values slightly over 10 for R1234ze(E) (the HFO that returned the best results in this study). The increase in *COP* with generator temperature is due to the reduction in the mass flow of the concentrated solution that needs to be heated. Once f stabilizes, an increase in generator temperature implies a reduction in the concentrated flow rate to be heated, but this does not compensate for the greater energy required to reach higher temperatures. In other words, the system becomes slightly less efficient as the generator temperature rises. In the case of CA-ARS, the compressor helps achieve an asymptotic value at lower generator temperatures, resulting in a better performance. Hence, CA-ARS clearly outperformed SE-ARS at low generator temperatures and the efficiency loss at high generator temperatures was still not enough to translate into a worse performance than SE-ARS.

Table 5.
Electrical *COP* for the different refrigerant gases.

Gas	COP_{el}
R32	11.86
R134a	13.39
R1234ze(E)	13.53
R1234yf	12.10

Fig. 7 shows the mass fraction increment between the absorber and desorber in CA-ARS and Table S8 in the Supplementary Information compiles the mass fraction of refrigerant in the absorber. As can be seen, ARS presented some operational limits at low generator temperatures corresponding to unfeasible situations in which the pressure and temperature conditions resulted in a lower refrigerant solubility in the absorber than the desorber (i.e., when $\Delta w \leq 0$). This restricts the ARS' correct operation when only very low-grade thermal energy is available. Moreover, a comparison between the mass fraction increments in CA-ARS and SE-ARS (Table S5) highlights the improvement achieved with CA-ARS compared to SE-ARS. For example, for the R32/[C_2mim][Tf_2N] pair, the mass fraction in the absorber of the SE-ARS configuration was 0.147, whereas the maximum mass fraction increment of CA-ARS was over 0.2. The pressurization of the refrigerant before entering the absorber increases the amount of refrigerant absorbed and, therefore, improves system performance.

If we compare ILs to organic solvents as absorbents, better results were reported with TEGDME in terms of circulation factors, with values of around 3, and mass fraction increments over 0.3 at temperatures above 373 K with refrigerants such as R32, R152 and R161 (Zhang et al., 2021). However, the overall maximum *COP* was slightly higher with the system R32/[C_2mim][Tf_2N] studied in this work. This contrast is because the generator temperature for the optimal working point is lower for ILs. The *ECOP* underlines this difference, as the maximum *ECOP* was lower than 0.25 for TEGDME systems and higher than 0.35 for the systems in this study. This difference translates directly into one of the key advantages of IL-based CA-ARS proposed in this work, the possibility of using low-grade waste heat.

Table 6 shows a comparative assessment of CA-ARS performances (*COP*, circulation factor, compressor power, and energy in each element) for the 16 pairs analyzed in this study for a refrigerant mass flow rate of 1 kg·s^{-1} and a low-grade heat source at 333 K. HFC-R32 pairs gave the best overall performances in terms of *COP* and f, whereas HFO-R1234yf based pairs were the poorest performers. Although the HFO R1234ze(E) exhibited lower *COPs* than R32, this very-low-GWP refrigerant significantly reduces the compressor power and has a similar refrigeration capacity (Q_e) as R134a, thus making it an attractive refrigerant in a low-cost IL production scenario.

5. Conclusion

Here we have presented the thermodynamic modeling and analysis of the performance of 16 novel working pairs formed from low-GWP HFC and very-low-GWP HFO refrigerant gasses combined with low-viscosity ILs. Additionally, we provide new experimental data on the solubility of R1234ze(E) in [C_2mim][Tf_2N], [C_2mim][OTf], and [C_2mim][SCN]. After comparing the results for single effect and compression assisted refrigeration systems, we conclude that:

(1) The solubility of R1234ze(E) in the selected ILs is significantly higher than that of previously studied HFOs, being much higher than its isomer R1234yf, and similar to the solubility of R134a. This makes R1234ze(E) an interesting refrigerant for absorption machines as its GWP is 1000 times lower.
(2) SE-ARS have medium to low performances and limitations in cooling with low-grade thermal energy. The best results are achieved with R32/[C_2mim][BF_4] with *COP* = 0.41 and f = 21.3 at a generator temperature of 348 K.

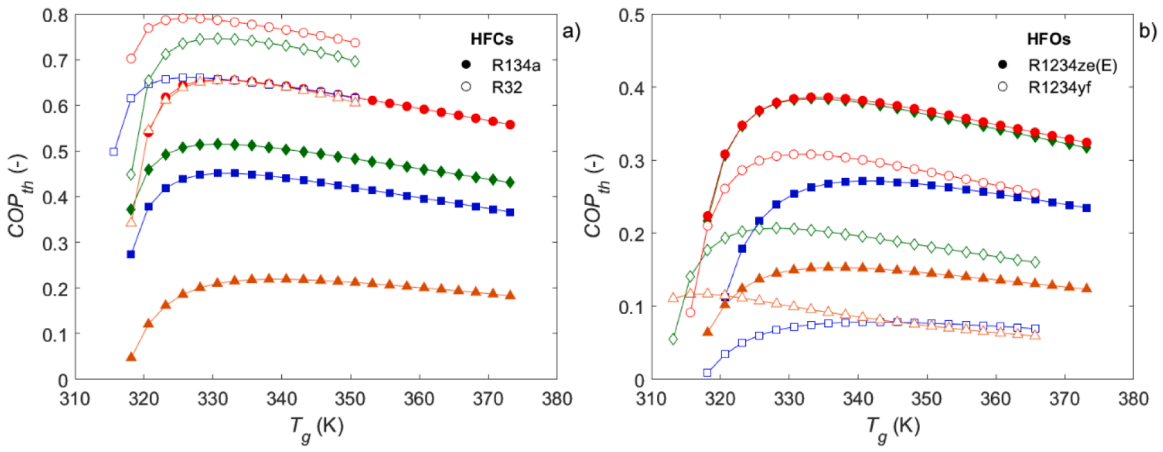

Fig. 4. Thermal *COP* of the CA-ARS systems as a function of generator temperature (T_g). (a) HFCs/IL: R134a (filled symbols) and R32 (empty symbols), and (b) HFOs/IL: R1234ze(E) (filled symbols) and R1234yf (empty symbols). Symbols represent the different ILs: [C_2mim][BF_4] (■), [C_2mim][OTf] (◆), [C_2mim][SCN] (▲), and [C_2mim][Tf_2N] (●). $T_e = 278$ K, $T_c = T_a = 303$ K.

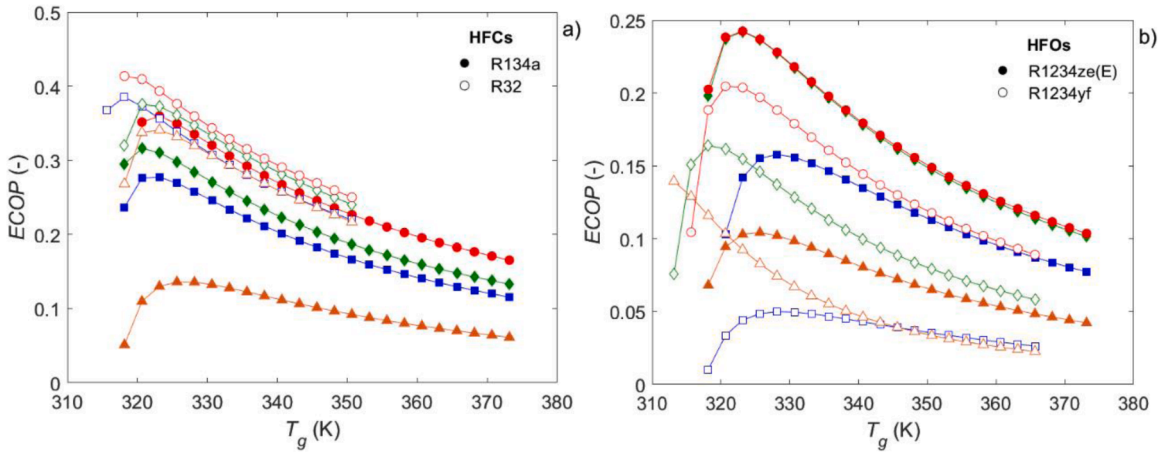

Fig. 5. *ECOP* of the CA-ARS systems as a function of generator temperature (T_g). (a) HFCs/IL: R134a (filled symbols) and R32 (empty symbols), and (b) HFOs/IL: R1234ze(E) (filled symbols) and R1234yf (empty symbols). Symbols represent the different ILs: [C_2mim][BF_4] (■), [C_2mim][OTf] (◆), [C_2mim][SCN] (▲), and [C_2mim][Tf_2N] (●). $T_e = 278$ K, $T_c = T_a = 303$ K.

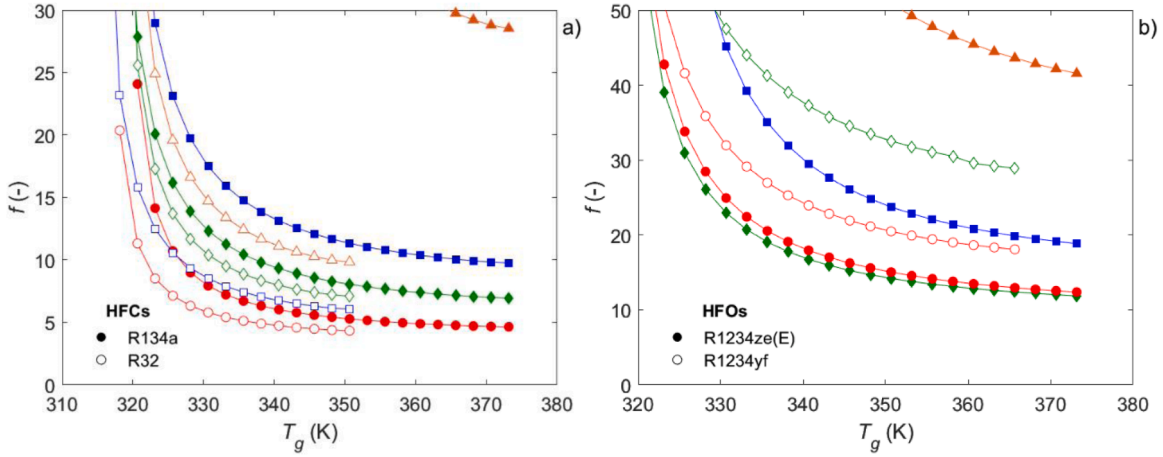

Fig. 6. Circulation factor (*f*) of the CA-ARS systems as a function of generator temperature (T_g). (a) HFCs/IL: R134a (filled symbols) and R32 (empty symbols), and (b) HFOs/IL: R1234ze(E) (filled symbols) and R1234yf (empty symbols). Symbols represent the different ILs: [C_2mim][BF_4] (■), [C_2mim][OTf] (◆), [C_2mim][SCN] (▲), and [C_2mim][Tf_2N] (●). $T_e = 278$ K, $T_c = T_a = 303$ K.

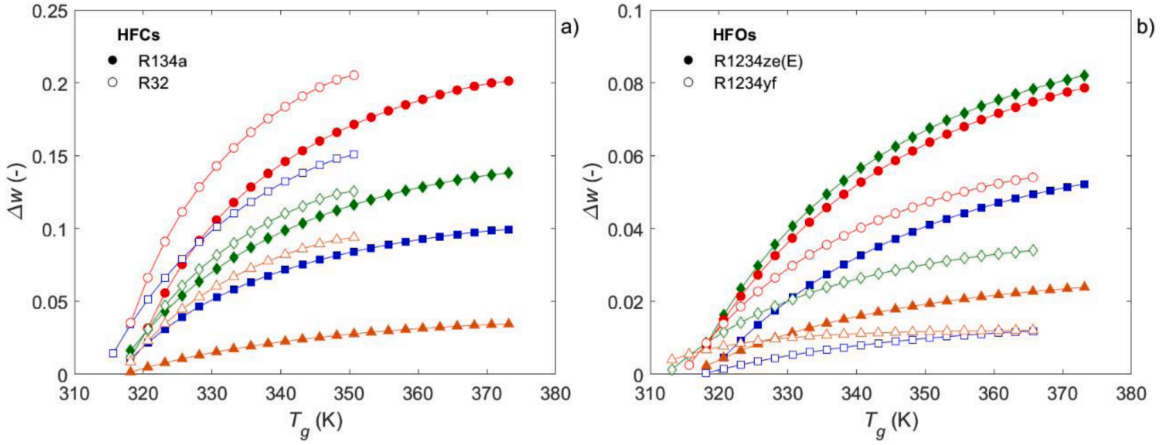

Fig. 7. Mass fraction increment (Δw) of the CA-ARS systems as a function of generator temperature (T_g). (a) HFCs/IL: R134a (filled symbols) and R32 (empty symbols), and (b) HFOs/IL: R1234ze(E) (filled symbols) and R1234yf (empty symbols). Symbols represent the different ILs: [C_2mim][BF_4] (■), [C_2mim][OTf] (◆), [C_2mim][SCN] (▲), and [C_2mim][Tf_2N] (●). T_e = 278 K, $T_c = T_a$ = 303 K.

Table 6.
Performance of the CA-ARS under the same conditions (T_e = 278 K, $T_c = T_a$ = 303 K, T_g = 333 K, CR = 1.5, m_r = 1 kg·s^{-1}).

Working Pair	f	Q_g (kW)	Q_e (kW)	Q_a (kW)	Q_c (kW)	W_{comp} (kW)	***COP***
R134a/[C_2mim][BF_4]	15.9	354.4	159.8	−329.5	−196.6	11.9	0.436
R134a/[C_2mim][OTf]	11.2	310.6	159.8	−286.5	−195.9	11.9	0.495
R134a/[C_2mim][SCN]	55.4	742.4	159.8	−716.7	−197.5	11.9	0.212
R134a/[C_2mim][Tf_2N]	7.2	243.9	159.8	−221.4	−194.2	11.9	0.624
R32/[C_2mim][BF_4]	7.9	398.5	260.8	−390.1	−291.1	22.0	0.620
R32/[C_2mim][OTf]	9.5	350.2	260.8	−341.7	−291.2	22.0	0.701
R32/[C_2mim][SCN]	13.4	398.9	260.8	−389.1	−292.5	22.0	0.620
R32/[C_2mim][Tf_2N]	5.4	333.4	260.8	−328.5	−287.8	22.0	0.734
R1234ze(E)/[C_2mim][BF_4]	39.2	559.1	146.8	−530.4	−186.4	10.9	0.258
R1234ze(E)/[C_2mim][OTf]	20.7	382.2	146.8	−353.9	−186.0	10.9	0.374
R1234ze(E)/[C_2mim][SCN]	76.9	965.4	146.8	−936.2	−186.9	10.9	0.150
R1234ze(E)/[C_2mim][Tf_2N]	22.4	380.4	146.8	−352.2	−185.9	10.9	0.375
R1234yf/[C_2mim][BF_4]	162.9	1681.8	126.0	−1651.4	−166.9	10.4	0.075
R1234yf/[C_2mim][OTf]	44.0	616.9	126.0	−586.9	−166.4	10.4	0.201
R1234yf/[C_2mim][SCN]	95.5	1320.2	126.0	−1289.1	−167.6	10.4	0.095
R1234yf/[C_2mim][Tf_2N]	29.1	409.2	126.0	−379.6	−166.1	10.4	0.300

(3) CA-ARS represents an important improvement in *COP* and expands the range of working temperatures compared to SE-ARS, which has cooling limitations using low-grade thermal energy in the generator. In CA-ARS, the increased absorber solubility leads to significant improvements in the circulation factor, even with low generator temperatures.
(4) High refrigerant solubility at ambient temperatures is the key consideration in ARS to minimize the amount of solvent used, as such, new working pairs with very-low-GWP HFOs, such as R1234ze(E), and ILs with higher absorption capacities and low viscosities should be examined further for their use in cooling applications.

Moreover, promising results have been obtained in CA-ARS. The most remarkable results with CA-ARS were:

(1) The pair R32/[C_2mim][Tf_2N] outperformed pairs reported previously, and it is competitive with the classic pairs of NH_3/H_2O and H_2O/LiBr. R32/[C_2mim][Tf_2N] presents a *COP* of 0.74, a circulation factor of 5.4 at 328 K in the desorber, and a maximum *ECOP* of 0.41 at 318 K. This pair is the most promising alternative of all the HFC or HFO/ionic liquid mixtures published to date for energy efficient cooling by absorption refrigeration technology.
(2) If we focus on using refrigerants with a negligible GWP, the HFO R1234ze(E) (GWP = 1) shows promising results in its pairs with [C_2mim][Tf_2N] and [C_2mim][OTf], with *COPs* of 0.37. They do not perform as well as HFC-based pairs, but they can be used when significant amounts of waste heat are available. In addition, the lower working pressure of R1234ze(E) compared to that of R32 reduces the compressor electricity demand.

Author contribution

José M. Asensio-Delgado: Investigation, Visualization, Writing - original draft. **Salvador Asensio-Delgado:** Investigation, conceptualization, Supervision, Writing - review & editing, original draft. **Gabriel Zarca:** Conceptualization, Writing - review & editing, Funding acquisition. **Ane Urtiaga:** Conceptualization, Writing - review & editing, Funding acquisition(Eq.10, Eq.11, Eq.12, Eq.13, Eq.14, Eq.15, Eq.16, Eq.19, Eq.20, Eq.21, Eq.22, Eq.2, Eq.3, Eq.4, Eq.5, Eq.6, Eq.7, Eq.8)

Declaration of Competing Interest

The authors declare no competing financial interest.

Acknowledgments

We gratefully acknowledge the support from projects KET4F-Gas-SOE2/P1/P0823 (Interreg SUDOE) and PID2019–105827RB-I00 (MCIN/AEI/10.13039/501100011033). S. A-D. acknowledges the FPU grant (18/03939) awarded by the Spanish MSIU.

References

Annual European Union Greenhouse Gas Inventory 1990-2018 and Inventory Report 2020, 2020. European Environment Agency, Brussels. https://www.eea.europa.eu/publications/european-union-greenhouse-gas-inventory-2020.

Seiler, M., Kühn, A., Ziegler, F., Wang, X., 2013. Sustainable cooling strategies using new chemical system solutions. Ind. Eng. Chem. Res. 52, 16519–16546. https://doi.org/10.1021/ie401297u.

Garcia, E.J., Bahamon, D., Vega, L.F., 2021. Systematic Search of Suitable Metal-Organic Frameworks for Thermal Energy-Storage Applications with Low Global Warming Potential Refrigerants. ACS Sustain. Chem. Eng. 9, 3157–3171. https://doi.org/10.1021/acssuschemeng.0c07797.

Gao, Y., He, G., Chen, P., Zhao, X., Cai, D., 2019. Energy and exergy analysis of an air-cooled waste heat-driven absorption refrigeration cycle using R290/oil as working fluid. Energy 173, 820–832. https://doi.org/10.1016/j.energy.2019.02.117.

Zhang, X., Cai, L., Chen, T., Qiao, J., Zhang, X., 2021. Vapor-Liquid Equilibrium Measurements and Assessments of Low-GWP Absorption Working Pairs (R32+DMETEG, R152a+DMETEG, and R161+DMETEG) for Absorption Refrigeration Systems. Energy 224, 120082. https://doi.org/10.1016/j.energy.2021.120082.

Asensio-Delgado, S., Viar, M., Pardo, F., Zarca, G., Urtiaga, A., 2021a. Gas solubility and diffusivity of hydrofluorocarbons and hydrofluoroolefins in cyanide-based ionic liquids for the separation of refrigerant mixtures. Fluid Phase Equilib 549, 113210. https://doi.org/10.1016/j.fluid.2021.113210.

Yokozeki, A., Shiflett, M.B., 2010. Water solubility in ionic liquids and application to absorption cycles. Ind. Eng. Chem. Res. 49, 9496–9503. https://doi.org/10.1021/ie1011432.

Kim, Y.J., Kim, S., Joshi, Y.K., Fedorov, A.G., Kohl, P.A., 2012. Thermodynamic analysis of an absorption refrigeration system with ionic-liquid/refrigerant mixture as a working fluid. Energy 44, 1005–1016. https://doi.org/10.1016/j.energy.2012.04.048.

Wang, M., Infante Ferreira, C.A., 2017. Absorption heat pump cycles with NH3 – ionic liquid working pairs. Appl. Energy. 204, 819–830. https://doi.org/10.1016/j.apenergy.2017.07.074.

Moreno, D., Ferro, V.R., de Riva, J., Santiago, R., Moya, C., Larriba, M., Palomar, J., 2018. Absorption refrigeration cycles based on ionic liquids: refrigerant/absorbent selection by thermodynamic and process analysis. Appl. Energy. 213, 179–194. https://doi.org/10.1016/j.apenergy.2018.01.034.

Asensio-Delgado, S., Jovell, D., Zarca, G., Urtiaga, A., Llovell, F., 2020a. Thermodynamic and process modeling of the recovery of R410A compounds with ionic liquids. Int. J. Refrig. 118, 365–375. https://doi.org/10.1016/j.ijrefrig.2020.04.013.

McLinden, M.O., Huber, M.L., 2020. (R)Evolution of Refrigerants. J. Chem. Eng. Data. 65, 4176–4193. https://doi.org/10.1021/acs.jced.0c00338.

Wu, W., You, T., Zhang, H., Li, X., 2018. Comparisons of different ionic liquids combined with trans-1,3,3,3-tetrafluoropropene (R1234ze(E)) as absorption working fluids. Int. J. Refrig. 88, 45–57. https://doi.org/10.1016/j.ijrefrig.2017.12.011.

Sun, Y., Di, G., Wang, J., Hu, Y., Wang, X., He, M., 2020a. Gaseous solubility and thermodynamic performance of absorption system using R1234yf /IL working pairs. Appl. Therm. Eng. 172, 115161 https://doi.org/10.1016/j.applthermaleng.2020.115161.

Sun, Y., Di, G., Wang, J., Wang, X., Wu, W., 2020b. Performance analysis of R1234yf/ionic liquid working fluids for single-effect and compression-assisted absorption refrigeration systems. Int. J. Refrig. 109, 25–36. https://doi.org/10.1016/j.ijrefrig.2019.10.007.

Liu, X., Ye, Z., Bai, L., He, M., 2019. Performance comparison of two absorption-compression hybrid refrigeration systems using R1234yf/ionic liquid as working pair. Energy Convers. Manag. 181, 319–330. https://doi.org/10.1016/j.enconman.2018.12.030.

Wu, W., Leung, M., Ding, Z., Huang, H., Bai, Y., Deng, L., 2020. Comparative analysis of conventional and low-GWP refrigerants with ionic liquid used for compression-assisted absorption cooling cycles. Appl. Therm. Eng. 172, 115145 https://doi.org/10.1016/j.applthermaleng.2020.115145.

Wu, W., Zhang, H., You, T., Li, X., 2017a. Performance comparison of absorption heating cycles using various low-GWP and natural refrigerants. Int. J. Refrig. 82, 56–70. https://doi.org/10.1016/j.ijrefrig.2017.07.004.

Wu, W., Zhang, H., You, T., Li, X., 2017b. Thermodynamic Investigation and Comparison of Absorption Cycles Using Hydrofluoroolefins and Ionic Liquid. Ind. Eng. Chem. Res. 56, 9906–9916. https://doi.org/10.1021/acs.iecr.7b02343.

Zarca, G., Ortiz, I., Urtiaga, A., 2014. Kinetics of the carbon monoxide reactive uptake by an imidazolium chlorocuprate(I) ionic liquid. Chem. Eng. J. 252, 298–304. https://doi.org/10.1016/j.cej.2014.05.011.

Zarca, G., Ortiz, I., Urtiaga, A., 2015. Recovery of carbon monoxide from flue gases by reactive absorption in ionic liquid imidazolium chlorocuprate(I): mass transfer coefficients. Chinese J. Chem. Eng. 23, 769–774. https://doi.org/10.1016/j.cjche.2014.06.040.

Mota-Martinez, M.T., Brandl, P., Hallett, J.P., Dowell, N.Mac, 2018. Challenges and opportunities for the utilisation of ionic liquids as solvents for CO2 capture. Mol. Syst. Des. Eng. 3, 560–571. https://doi.org/10.1039/c8me00009c.

Palomar, J., Larriba, M., Lemus, J., Moreno, D., Santiago, R., Moya, C., de Riva, J., Pedrosa, G., 2019. Demonstrating the key role of kinetics over thermodynamics in the selection of ionic liquids for CO2 physical absorption. Sep. Purif. Technol. 213, 578–586. https://doi.org/10.1016/j.seppur.2018.12.059.

Sanmamed, Y.A., González-Salgado, D., Troncoso, J., Romani, L., Baylaucq, A., Boned, C., 2010. Experimental methodology for precise determination of density of RTILs as a function of temperature and pressure using vibrating tube densimeters. J. Chem. Thermodyn. 42, 553–563. https://doi.org/10.1016/j.jct.2009.11.014.

Neves, C.M.S.S., Kurnia, K.A., Coutinho, J.A.P., Marrucho, I.M., Canongia Lopes, J.N., Freire, M.G., Rebelo, L.P.N., 2013. Systematic study of the thermophysical properties of imidazolium-based ionic liquids with cyano-functionalized anions. J. Phys. Chem. B. 117, 10271–10283. https://doi.org/10.1021/jp405913b.

Gardas, R.L., Costa, H.F., Freire, M.G., Carvalho, P.J., Marrucho, I.M., Fonseca, I.M.A., Ferreira, A.G.M., Coutinho, J.A.P., 2008. Densities and derived thermodynamic properties of imidazolium-, pyridinium-, pyrrolidinium-, and piperidinium-based ionic liquids. J. Chem. Eng. Data. 53, 805–811. https://doi.org/10.1021/je700670k.

European Commission, 2020. Mapping and analyses of the current and future (2020 - 2030) heating/cooling fuel deployment (fossil/renewables). European Commission. https://ec.europa.eu/energy/studies_main/final_studiesmapping-and-analyses-current-and-future-2020-2030-heatingcooling-fuel.

Freire, M.G., Teles, A.R.R., Rocha, M.A.A., Schröder, B., Neves, C.M.S.S., Carvalho, P.J., Evtuguin, D.V., Santos, L.M.N.B.F., Coutinho, J.A.P., 2011. Thermophysical Characterization of Ionic Liquids Able To Dissolve Biomass. J. Chem. Eng. Data. 56, 4813–4822. https://doi.org/10.1021/je200790q.

Součková, M., Klomfar, J., Pátek, J., 2014. Measurements and group contribution analysis of 0.1 MPa densities for still poorly studied ionic liquids with the [PF6] and [NTf2] anions. J. Chem. Thermodyn. 77, 31–39. https://doi.org/10.1016/j.jct.2014.04.017.

ASHRAE, 2013. ASHRAE Handbook—Fundamentals. 2013 ASHRAE Handbook—Fundamentals.

Atilhan, M., Jacquemin, J., Rooney, D., Khraisheh, M., Aparicio, S., 2013. Viscous behavior of imidazolium-based ionic liquids. Ind. Eng. Chem. Res. 52, 16774–16785. https://doi.org/10.1021/ie403065u.

Asensio-Delgado, S., Pardo, F., Zarca, G., Urtiaga, A., 2020b. Vapor−Liquid Equilibria and Diffusion Coefficients of Difluoromethane, 1,1,1,2-Tetrafluoroethane, and 2,3,3,3-Tetrafluoropropene in Low-Viscosity Ionic Liquids. J. Chem. Eng. Data. 65, 4242–4251. https://doi.org/10.1021/acs.jced.0c00224.

Bell, I.H., Wronski, J., Quoilin, S., Lemort, V., 2014. Pure and Pseudo-pure Fluid Thermophysical Property Evaluation and the Open-Source Thermophysical Property Library CoolProp. Ind. Eng. Chem. Res. 53, 2498–2508. https://doi.org/10.1021/ie4033999.

Waliszewski, D., Stępniak, I., Piekarski, H., Lewandowski, A., 2005. Heat capacities of ionic liquids and their heats of solution in molecular liquids. Thermochim. Acta. 433, 149–152. https://doi.org/10.1016/j.tca.2005.03.001.

Diedrichs, A., Gmehling, J., 2006. Measurement of heat capacities of ionic liquids by differential scanning calorimetry. Fluid Phase Equilib 244, 68–77. https://doi.org/10.1016/j.fluid.2006.03.015.

Zorębski, E., Musiał, M., Bałuszyńska, K., Zorębski, M., Dzida, M., 2018. Isobaric and Isochoric Heat Capacities as Well as Isentropic and Isothermal Compressibilities of Di- and Trisubstituted Imidazolium-Based Ionic Liquids as a Function of Temperature. Ind. Eng. Chem. Res. 57, 5161–5172. https://doi.org/10.1021/acs.iecr.8b00506.

Takalkar, G.D., Bhosale, R.R., Mali, N.A., Bhagwat, S.S., 2019. Thermodynamic analysis of EMISE–Water as a working pair for absorption refrigeration system. Appl. Therm. Eng. 148, 787–795. https://doi.org/10.1016/j.applthermaleng.2018.11.092.

Asensio-Delgado, S., Pardo, F., Zarca, G., Urtiaga, A., 2020c. Enhanced absorption separation of hydrofluorocarbon/hydrofluoroolefin refrigerant blends using ionic liquids. Sep. Purif. Technol. 249, 117136 https://doi.org/10.1016/j.seppur.2020.117136.

Shiflett, M.B., Yokozeki, A., 2007. Solubility Differences of Halocarbon Isomers in Ionic Liquid [emim][Tf2N]. J. Chem. Eng. Data. 52, 2007–2015. https://doi.org/10.1021/je700295e.

Dong, L., Zheng, D., Sun, G., Wu, X., 2011. Vapor-Liquid Equilibrium Measurements of Difluoromethane + [Emim]OTf, Difluoromethane + [Bmim]OTf, Difluoroethane + [Emim]OTf, and Difluoroethane + [Bmim]OTf Systems. J. Chem. Eng. Data. 56, 3663–3668. https://doi.org/10.1021/je2005566.

Shiflett, M.B., Harmer, M.A., Junk, C.P., Yokozeki, A., 2006. Solubility and Diffusivity of Difluoromethane in Room-Temperature Ionic Liquids. J. Chem. Eng. Data. 51, 483–495. https://doi.org/10.1021/je050386z.

Sun, Y., Zhang, Y., Wang, X., Prausnitz, J.M., Jin, L., 2017. Gaseous absorption of 2,3,3,3-tetrafluoroprop-1-ene in three imidazolium-based ionic liquids. Fluid Phase Equilib 450, 65–74. https://doi.org/10.1016/j.fluid.2017.07.013.

He, M., Peng, S., Liu, X., Pan, P., He, Y., 2017. Diffusion coefficients and Henry's constants of hydrofluorocarbons in [HMIM][Tf2N, HMIM][TfO], and [HMIM][BF4]. J. Chem. Thermodyn. 112, 43–51. https://doi.org/10.1016/j.jct.2017.04.009.

Asensio-Delgado, S., Pardo, F., Zarca, G., Urtiaga, A., 2021b. Absorption separation of fluorinated refrigerant gases with ionic liquids: equilibrium, mass transport, and process design. Sep. Purif. Technol. 276, 119363 https://doi.org/10.1016/j.seppur.2021.119363.

Kühn, R., Meyer, T., Ziegler, F., 2020. Experimental investigation of ionic liquids as substitute for lithium bromide in water absorption chillers. Energy 205, 117990. https://doi.org/10.1016/j.energy.2020.117990.